

ARTop: an open-source tool for measuring active region topology at the solar photosphere

K. Alielden,¹ D. MacTaggart¹,²★ Q. Ming,^{3,4} C. Prior⁵ and B. Raphaldini^{5,6}

¹*School of Mathematics and Physics, Aberystwyth University, Ceredigion SY23 3BZ, UK*

²*School of Mathematics and Statistics, University of Glasgow, Glasgow G12 8QQ, UK*

³*Institute for Space-Earth Environmental Research, Nagoya University, Nagoya 464-8601, Japan*

⁴*School of Earth and Space Sciences, University of Science and Technology of China, Hefei 230026, China*

⁵*Department of Mathematical Sciences, Durham University, Durham DH1 3LE, UK*

⁶*High Altitude Observatory, NCAR, 3080 Center Green Drive, Boulder, CO 80301, USA*

Accepted 2023 July 10. Received 2023 June 21; in original form 2022 November 3

ABSTRACT

The importance of measuring topological quantities, such as magnetic helicity, in solar observations has long been recognized. In particular, topological quantities play an important role in both understanding and predicting solar eruptions. In this paper, we present ARTop (Active Region Topology), an open-source and end-to-end software tool that allows researchers to calculate the fluxes of topological quantities based on solar magnetograms. In addition to this, ARTop also allows for the efficient analysis of these quantities in both 2D maps and time series. ARTop calculates the fluxes of magnetic helicity and magnetic winding, together with particular decompositions of these quantities. To perform these calculations, SHARP magnetograms are downloaded and velocity maps are created using the DAVE4VM method. Visualization tools, written in Python, are provided to aid in the selection of appropriate output variables and for the straightforward creation of maps and time series. Additionally, other analysis functions are included to facilitate and aid solar flare investigations. This software offers researchers a powerful tool for investigating the behaviour of active regions and the origins of space weather.

Key words: numerical methods – software – magnetic helicity – magnetic winding – solar active regions.

1 INTRODUCTION

The evolution of solar active regions is characterized by the development of topologically complex magnetic field (e.g. van Driel-Gesztelyi & Green 2015). The word ‘topological’ here indicates the entanglement of magnetic field lines, and we will specify what this means shortly. Topologically complex magnetic field both emerges into the solar atmosphere through the photosphere, and can also be created by the braiding of the footpoints of the emerged field at the photosphere (e.g. Amari et al. 2003; Toriumi et al. 2013; Candelaresi et al. 2018; MacTaggart et al. 2021).

Reliable direct measurements of the solar magnetic field are only available at the photosphere, whereas the structure of the 3D field in the solar atmosphere requires additional modelling assumptions for its construction and estimation. Nonetheless, it is possible to estimate the flux, through the photosphere, of quantities related to the magnetic field that provide information about the emerging field’s topology. One of the most prominent measures of magnetic field topology is relative magnetic helicity, and measurements of the flux of this quantity in solar magnetograms have become a staple of active region analysis over the past 20 yr (e.g. Chae 2001; Yamamoto et al. 2005; Jeong & Chae 2007; LaBonte, Georgoulis & Rust 2007; Yang, Zhang & Büchner 2009; Chandra et al. 2010; Liu & Schuck 2012;

Park et al. 2012; Liu et al. 2014; Romano et al. 2014; Vemareddy & Démoulin 2017). A review of numerical techniques for calculating magnetic helicity in simulations and observations can be found in Parlat (2020).

Another important topological quantity that can be estimated from magnetograms is magnetic winding (MacTaggart et al. 2021). Although we described magnetic helicity as a topological quantity, it actually combines two fundamental quantities: magnetic topology and magnetic flux. Magnetic winding is a renormalization of magnetic helicity that provides direct information about the field line entanglement, i.e. it removes any possible confound on topological information created by weighting field lines with their field strength. As the name suggests, the underlying topology of magnetic field lines is measured by their winding about each other (Berger 1993; Candelaresi et al. 2021). This generalizes the concept of field line linkage in classical helicity (Prior & Yeates 2014; Prior & MacTaggart 2020). Magnetic winding can be shown to provide distinct information compared to magnetic helicity in observational studies. It has proven to be an important quantity for identifying the source of current-carrying magnetic structure (a twisted flux tube) in the solar atmosphere (MacTaggart et al. 2021).

In this work, we present an open-source software package called ARTop. This stands for Active Region Topology, and it is designed to calculate and analyse magnetic helicity and magnetic winding, together with important decompositions of these quantities. This

* E-mail: david.mactaggart@glasgow.ac.uk

package provides the user with simple functionality to study the topology of active regions from the downloading of magnetograms through to the analysis of topological quantities and their relation to the onset of flares. The paper is outlined as follows. The next section describes the topological quantities that are calculated in ARTop. We then describe the structure of the algorithm and present illustrative examples of the code's analysis routines. Finally, we assess the influence of key parameters in ARTop. While this article provides an overview of the underlying theory and capabilities of ARTop, code documentation can be found with the source code.¹

2 TOPOLOGICAL QUANTITIES

The topological quantities calculated in ARTop are based on magnetic fields passing through or evolving on a horizontal and static plane P that represents a rectangular subset of the photosphere. The magnetic field distribution on P will be provided by Space-Weather Helioseismic and Magnetic Imager (HMI) Active Region Patches (SHARP) vector magnetograms (Hoeksema et al. 2014). Although a flat and static plane is an approximation of the photospheric boundary, simulations suggest that it is a reasonable assumption for the calculation of magnetic helicity and magnetic winding (Prior & MacTaggart 2019; MacTaggart & Prior 2021).

As mentioned in the introduction, field line winding represents the topological description of the magnetic field that underlines both magnetic helicity and magnetic winding. Let $\mathbf{x}(t) = (x_1, x_2)$ and $\mathbf{y}(t) = (y_1, y_2)$ represent the position vectors in P of two field lines intersecting P at a time t . The mutual angle $\Theta(\mathbf{x}, \mathbf{y})$ of the two field line intersection points in P is given by

$$\Theta(\mathbf{x}, \mathbf{y}) = \arctan\left(\frac{y_2 - x_2}{y_1 - x_1}\right). \quad (1)$$

The vector $\mathbf{u}(\mathbf{y}) = (dy_1/dt, dy_2/dt)$ is the planar velocity of the field line footpoint indicated by \mathbf{y} , and is referred to as the field line velocity. Writing $\mathbf{r} = \mathbf{y} - \mathbf{x}$, the time derivative of equation (1) can be expressed as

$$\frac{d\Theta}{dt} = \mathbf{e}_z \cdot \frac{(\mathbf{u}(\mathbf{x}) - \mathbf{u}(\mathbf{y})) \times \mathbf{r}}{|\mathbf{r}|^2}, \quad (2)$$

where \mathbf{e}_z is the unit vector orthogonal to P . Equation (2) represents the basic building block of the underlying topological description of the fluxes that we will calculate – the pairwise winding of field lines (e.g. Candelaresi et al. 2021). We define a winding kernel based on equation (2) in order to define subcomponents of the winding/helicity fluxes,

$$K[\mathbf{u}_1, \mathbf{u}_2; \mathbf{x}, \mathbf{y}, t] = \frac{1}{2\pi} \mathbf{e}_z \cdot \frac{(\mathbf{u}_2(\mathbf{x}) - \mathbf{u}_1(\mathbf{y})) \times \mathbf{r}}{|\mathbf{r}|^2}, \quad (3)$$

where \mathbf{u}_1 and \mathbf{u}_2 will change depending on what quantity is calculated. Henceforth, for brevity, we will omit showing the dependence of K on quantities that come after the semicolon. Derivations of the topological quantities that we calculate here are treated in other works (e.g. Prior & Yeates 2014; Prior & MacTaggart 2020). Here, instead, we list the various quantities that are built on the winding kernel K .

2.1 Helicity fluxes

The field line helicity input rate, $d\mathcal{H}/dt$, that is, the helicity input rate relative to a field line indicated by \mathbf{x} , is

$$\frac{d\mathcal{H}}{dt}(\mathbf{x}) = -B_z(\mathbf{x}) \int_P B_z(\mathbf{y}) K[\mathbf{u}(\mathbf{x}), \mathbf{u}(\mathbf{y})] d^2y. \quad (4)$$

It should be noted that the above definition of the field line helicity rate is different from some others that are used in the literature (e.g. Berger 1988). The rate of total magnetic helicity flux, dH/dt , is then the integral of equation (4) over P , i.e.

$$\frac{dH}{dt} = - \int_P \int_P B_z(\mathbf{x}) B_z(\mathbf{y}) K[\mathbf{u}(\mathbf{x}), \mathbf{u}(\mathbf{y})] d^2x d^2y. \quad (5)$$

Equation (5) shows clearly how the magnetic helicity flux is a combination of information about magnetic flux and field line topology (see Prior & MacTaggart 2020, for a more detailed discussion).

2.1.1 Decompositions

Equations (4) and (5) represent the two topological quantities that have been calculated in many previous works. We now consider two further decompositions. First, the field line velocity can be decomposed (Berger 1988; Démoulin & Berger 2003; Pariat, Démoulin & Berger 2005) as

$$\begin{aligned} \mathbf{u}(\mathbf{x}) &= \mathbf{v}_{\parallel}(\mathbf{x}) - \frac{v_z(\mathbf{x})}{B_z(\mathbf{x})} \mathbf{B}_{\parallel}(\mathbf{x}), \\ &= \mathbf{u}_b + \mathbf{u}_e, \end{aligned} \quad (6)$$

where $\mathbf{u}_b := \mathbf{v}_{\parallel}$ is the braiding velocity (due to the horizontal motion of footpoints in P) and $\mathbf{u}_e := -(v_z/B_z)\mathbf{B}_{\parallel}$ is the emergence velocity (due to the emergence or submergence of a field line changing the position of the footpoint in P). Please note that the notation with a subscript \parallel refers to vectors parallel to P (i.e. horizontal vectors on the photosphere) and not vectors parallel to the magnetic field (for which this notation is sometimes used in the literature). The vector \mathbf{v} is the plasma velocity (or the flux-conserving velocity if other non-resistive terms are included in Ohm's law). Representations of how the braiding and emerging velocities affect the field line winding are displayed in Fig. 1.

With this decomposition, we can determine helicity fluxes due to braiding and emergence velocities individually. For example, if we wanted to find the field line helicity rate due to the braiding velocity alone, the only change to equation (4) would be in the winding kernel,

$$\frac{d\mathcal{H}_b}{dt}(\mathbf{x}) = -B_z(\mathbf{x}) \int_P B_z(\mathbf{y}) K[\mathbf{u}_b(\mathbf{x}), \mathbf{u}_b(\mathbf{y})] d^2y.$$

The second decomposition that we will consider is the splitting of the magnetogram magnetic field into a potential part and a 'current-carrying' part, i.e.

$$\mathbf{B}(t) = \mathbf{B}_p(t) + \mathbf{B}_c(t). \quad (7)$$

The idea is to split the current-carrying components, which are related to the free energy of the field, from potential components. In terms of helicity fluxes, the decomposition in (7) allows for more choices. To construct these, first note that $\mathbf{B} \cdot \mathbf{e}_z = \mathbf{B}_p \cdot \mathbf{e}_z$, so \mathbf{B}_c is a planar vector field. This means that the field line velocity decomposition in equation (6) becomes

$$\mathbf{u}(\mathbf{x}) = \mathbf{v}_{\parallel}(\mathbf{x}) - \frac{v_z(\mathbf{x})}{B_z(\mathbf{x})} \mathbf{B}_{\parallel p}(\mathbf{x}) - \frac{v_z(\mathbf{x})}{B_z(\mathbf{x})} \mathbf{B}_{\parallel c}(\mathbf{x}). \quad (8)$$

The field line velocities for the potential and current-carrying parts

¹<https://github.com/DavidMacT/ARTop>

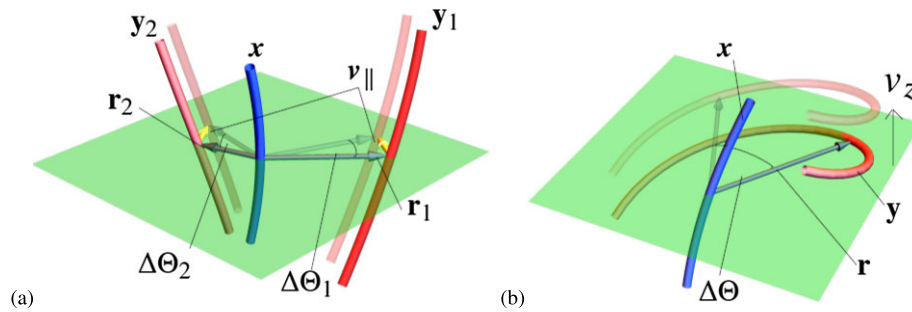


Figure 1 Field line winding due to (a) braiding on the photosphere and (b) emergence through the photosphere. In panel (a) the blue field line x intersects the photospheric plane, and two other field lines y_1, y_2 also pierce the plane. The vectors r_1 and r_2 join the intersection points of their field lines and x . The in-plane plasma velocity v_{\parallel} (shown as yellow arrows) indicates a motion of the field lines y_1, y_2 due to being ‘stirred’ or ‘braided’ by the plasma (under ideal motion). This motion leads to the vectors r_1 and r_2 subtending changes in angle $\Delta\Theta_1$ and $\Delta\Theta_2$ with respect to x . The winding measures this rotation and we refer to the change due to this in-plane motion as *braiding motion*. In panel (b) we see a helical field line y rising up through the photosphere (at velocity v_z), the kinked shape means there is apparent foot-point motion and rotation between the curves x and y , which can also be tracked by the variation in the change $\Delta\Theta$ in angle $\Theta(x, y)$ subtended by the two curves. We refer to this motion as *emergence motion* (which also includes submergence).

of the magnetic field are defined as

$$\mathbf{u}_p(\mathbf{x}) = \mathbf{v}_{\parallel}(\mathbf{x}) - \frac{v_z(\mathbf{x})}{B_z(\mathbf{x})} \mathbf{B}_{\parallel p}(\mathbf{x}), \tag{9}$$

$$\mathbf{u}_c(\mathbf{x}) = \mathbf{v}_{\parallel}(\mathbf{x}) - \frac{v_z(\mathbf{x})}{B_c(\mathbf{x})} \mathbf{B}_{\parallel c}(\mathbf{x}). \tag{10}$$

Since B_c is planar, its field line velocity is equivalent to that of the total magnetic field \mathbf{B} . Both equations (9) and (10) can be decomposed into braiding and emergence components, as before. Thus, with the above framework, it is straightforward to calculate the various decompositions by simply selecting the appropriate velocity fields to insert into the winding kernel.

2.1.2 δ -measure

With the braiding/emergence and potential/current-carrying decompositions established, we now present a particular measure that provides information about how the helicity due to the current-carrying part of the magnetic field compares to that due to the potential part of the magnetic field. This new measure, δH , is defined by

$$\delta H = \int_0^T \int_P \left(\left| \frac{d\mathcal{H}_c}{dt} \right| - \left| \frac{d\mathcal{H}_p}{dt} \right| \right) d^2y dt, \tag{11}$$

where T is some specified time. The flux of δH , which is calculated first in practice, is

$$\frac{d(\delta H)}{dt} = \int_P \left(\left| \frac{d\mathcal{H}_c}{dt} \right| - \left| \frac{d\mathcal{H}_p}{dt} \right| \right) d^2y. \tag{12}$$

This measure has the benefit of the stability of a global quantity (an integral over P) together with preserving the importance of local information (the subtraction of absolute values means that information is not lost upon integration over P). In brief, it indicates when the field line topology is dominated by the current-carrying component (it is positive) or the potential component (it is negative). Later, we will show one possible way in which the δ -measure may be used in relation to flare studies.

2.2 Winding fluxes

The decompositions described above for the magnetic helicity fluxes (4) and (5), also hold for magnetic winding fluxes. We will not repeat the description but only define the main winding fluxes. From these,

the construction of the various decompositions occurs in exactly the same manner as described previously.

Analogous to the field line helicity rate, the field line winding rate is given by

$$\frac{d\mathcal{L}}{dt}(\mathbf{x}) = -\sigma_z(\mathbf{x}) \int_P \sigma_z(\mathbf{y}) K[\mathbf{u}(\mathbf{x}), \mathbf{u}(\mathbf{y})] d^2y. \tag{13}$$

Equation (13) is identical to equation (4) but for the fact that B_z has been replaced by an indicator function σ_z , which is defined as

$$\sigma_z(\mathbf{x}) = \begin{cases} 1 & \text{if } B_z > 0, \\ -1 & \text{if } B_z < 0, \\ 0 & \text{if } B_z = 0. \end{cases} \tag{14}$$

Equation (14) describes the direction of a field line through P . It is this renormalization of the field strength that allows magnetic winding to be a direct measure of magnetic topology (MacTaggart et al. 2021). The rate of magnetic winding flux, dL/dt , is given by

$$\frac{dL}{dt} = - \int_P \int_P \sigma_z(\mathbf{x}) \sigma_z(\mathbf{y}) K[\mathbf{u}(\mathbf{x}), \mathbf{u}(\mathbf{y})] d^2x d^2y. \tag{15}$$

Finally there is the δL quantity

$$\delta L = \int_0^T \int_P \left(\left| \frac{d\mathcal{L}_c}{dt} \right| - \left| \frac{d\mathcal{L}_p}{dt} \right| \right) d^2y dt, \tag{16}$$

and its flux

$$\frac{d(\delta L)}{dt} = \int_P \left(\left| \frac{d\mathcal{L}_c}{dt} \right| - \left| \frac{d\mathcal{L}_p}{dt} \right| \right) d^2y, \tag{17}$$

where the same current-carrying/potential field decomposition, as described above, has been used.

3 ARTOP ALGORITHM

With the main topological quantities in place, we now describe the main stages of the ARTOP algorithm. Fig. 2 displays the main pipeline of ARTOP and this is followed by an overview of the main steps. Specific details required to install and run the code can be found in the online documentation.

3.1 Step 1: Setup

After downloading ARTOP, and assuming all the necessary dependencies are installed (these are detailed in the online documentation),

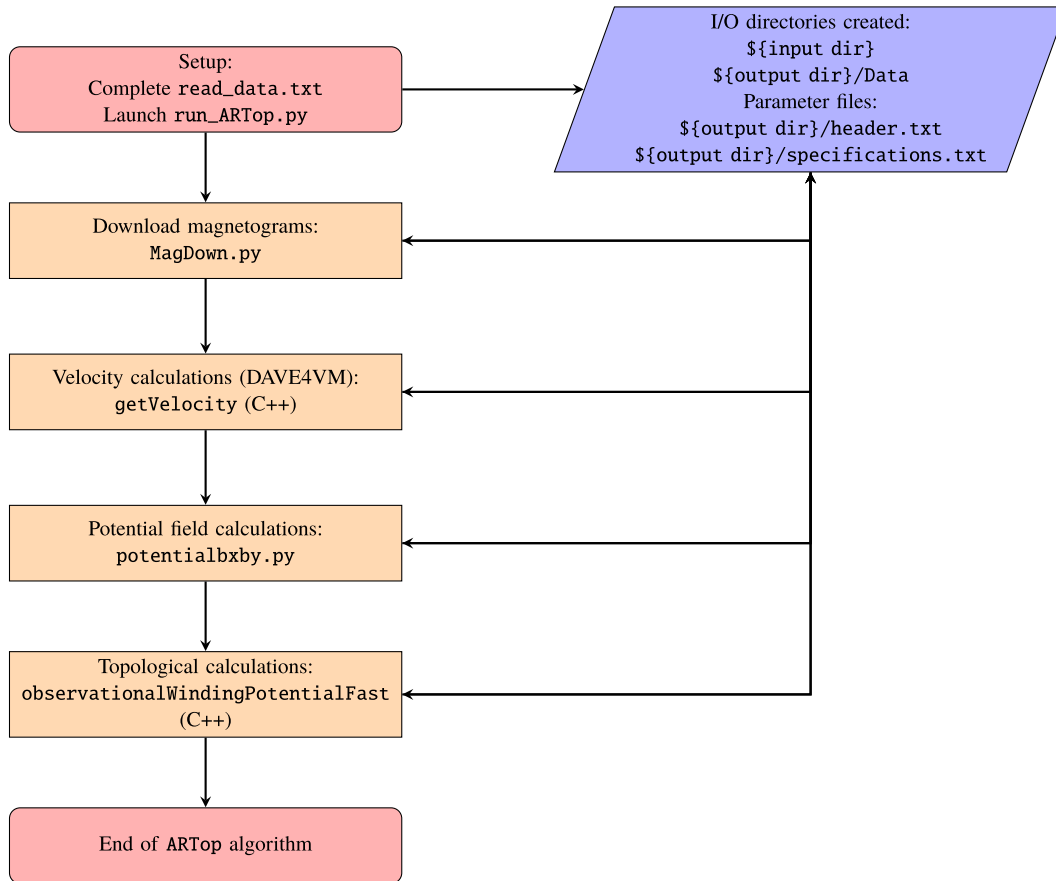


Figure 2 The algorithm of ARTop. For each of the steps, the main script/executable associated with that step is labelled. Bi-directional arrows indicate communication in both directions – all the main steps either read from or write to the input/output directories.

the user first needs to compile the C++ part of the code by running a makefile. The user then specifies details about the active region in `read_data.txt`. Once the necessary input parameters are inserted, the code is executed by running `run_ARTop.py`.

3.2 Step 2: Magnetogram downloads

While, in practice, a user would specify all input parameters before running the code (i.e. in Step 1), for ease of description, we refer to particular input parameters when describing the part of the algorithm to which they are associated.

The ARTop code obtains magnetic field data (the components of the field \mathbf{B}) for the appropriate active region by downloading, via `drms` (Glogowski et al. 2019), the CEA `hmi.sharp_cea_720s` product for that region (see Bobra et al. 2014). The download makes use of the `url-tar` method, in which a single `tar` file containing the necessary FITS files is downloaded and unpacked. Once the code has read all the FITS files and produced files of the magnetic field components in the format necessary for the next step of the algorithm, the FITS files are deleted (but the downloaded `tar` file remains and can be reused if needed).

The magnetic field data are mapped using the Lambert equal area cylindrical mapping which gives components (B_r, B_ϕ, B_θ) . These (point) values can then be identified with Cartesian components through the correspondence $B_z = B_r$, $B_x = B_\phi$, $B_y = -B_\theta$. The negative sign for the y -component accounts for the camera image inversion. We rely on the inbuilt 180-degree field disambiguation

provided automatically for the product via a minimum energy method (Metcalf 1994; Leka et al. 2009).

The SHARP number of the active region to be studied, plus the start and end times for the search, are the basic requirements for downloading magnetograms. Often, the SHARP number of an active region is not known a priori, but the National Oceanic and Atmospheric (NOAA) number is. ARTop includes a script for finding the SHARP number of an active region for a given NOAA number.

At this stage, the code also produces two auxiliary files, `header.txt` and `specifications.txt`, that are used by many parts of the algorithm. The first file contains header information relating to the downloaded magnetograms, and is needed for the visualization routines. The second auxiliary file contains the active region number, the magnetogram resolution, the number of time dumps and the values of three parameters (the smoothing factor, the cut-off, and the downsampling factor) which are discussed later.

3.3 Step 3: velocity calculations

Velocities are determined using the Differential Affine Velocity Estimator for Vector Magnetograms (DAVE4VM), developed by Schuck (2008). A C++ version of this algorithm has been implemented to speed up the calculations, which is a direct translation of the original IDL code. Thus the effectiveness of the method is identical to that demonstrated in Schuck (2008) (where results were compared to real velocity fields and anelastic 3D models). This method has become standard in the field (e.g. Liu & Team 2011; Romano et al. 2014;

Table 1. Spatially varying quantities output by ARTop.

Description	Symbol
Normal component of magnetic field	B_z
Normal field line velocity component	u_z
Normal Poynting flux	$S_z (= \mathbf{e}_z \cdot (\mathbf{E} \times \mathbf{B}))$
Field line winding rate	$d\mathcal{L}/dt$
Current-carrying field line winding rate	$d\mathcal{L}_c/dt$
Potential field line winding rate	$d\mathcal{L}_p/dt$
Braiding field line winding rate	$d\mathcal{L}_b/dt$
Field line helicity rate	$d\mathcal{H}/dt$
Current-carrying field line helicity rate	$d\mathcal{H}_c/dt$
Potential field line helicity rate	$d\mathcal{H}_p/dt$
Braiding field line helicity rate	$d\mathcal{H}_b/dt$
δ -measure winding rate integrand	$ d\mathcal{L}_c/dt - d\mathcal{L}_p/dt $
δ -measure helicity rate integrand	$ d\mathcal{H}_c/dt - d\mathcal{H}_p/dt $

Tziotziou et al. 2015; Vemareddy & Démoulin 2017). The velocity components are determined at each time only if two consecutive sets (x -, y -, and z -components) of magnetograms exist. If two consecutive sets do not exist, the code skips to the next time when two consecutive sets do exist. This can be seen in time series of the outputted variables as regions of zero (for flux data) or flat regions (for time-integrated data), see figs 2 and 6 of MacTaggart et al. (2021) for clear examples of the effects of missing data.

An important input parameter for the velocity calculations is the size of the smoothing window which is used to generate differentiable data sets from the noisy magnetogram data. This value is specified in pixels. Recommendations on what values to use are discussed in Schuck (2008), but the choices of 11 or 20 pixels are typical in the literature (e.g. Romano et al. 2014; MacTaggart et al. 2021). We show later the effect of varying this parameter.

3.4 Step 4: potential field calculations

In order to perform the decomposition in equation (7), the x - and y -components of \mathbf{B}_p must be determined. This is performed efficiently in a Python script, for every time step, using a Fourier series decomposition, as described in Gary (1989) (a linear force-free method from which we take the potential case). This method implicitly assumes periodicity in the data, which is reasonable for SHARP data sets where the field is significantly weak at the boundary of the domain. It also matches a periodic assumption made in a least square fit derivative estimate of the field in the DAVE4VM method.

3.5 Step 5: Topological calculations

The stages described previously have been in preparation for the main calculations of ARTop. Table 1 lists all the quantities that are either taken from previous calculations or calculated at this stage. For each time dump, there is a file with these variables as columns.

All of the variables in Table 1 are spatial quantities, i.e. they vary over P . Note that the emergence fluxes, although not listed explicitly, can be calculated as $d\mathcal{L}/dt - d\mathcal{L}_b/dt$ and $d\mathcal{H}/dt - d\mathcal{H}_b/dt$.

At the end of each output file, there are ten variables with spatially integrated quantities. These are displayed in Table 2.

The quantities in this stage are calculated using a C++ code with OpenMP. Quantities based on quadrature are determined with a standard midpoint rule, which is fast and suitable for the smoothness of the magnetogram data.

An important input parameter for this stage is the downsampling number. This parameter allows for much faster calculations by

Table 2. Spatially integrated quantities output by ARTop.

Description	Symbol
Current-carrying winding rate	$d\mathcal{L}_c/dt$
Potential winding rate	$d\mathcal{L}_p/dt$
Braiding winding rate	$d\mathcal{L}_b/dt$
Current-carrying helicity rate	$d\mathcal{H}_c/dt$
Potential helicity rate rate	$d\mathcal{H}_p/dt$
Braiding helicity rate	$d\mathcal{H}_b/dt$
Total winding rate	$d\mathcal{L}/dt$
Total helicity rate	$d\mathcal{H}/dt$
δ -measure winding rate	$d(\delta\mathcal{L})/dt$
δ -measure helicity rate	$d(\delta\mathcal{H})/dt$

reducing the resolution of calculations. Later, we will provide a description of how this is achieved in ARTop without sacrificing the behaviour of important features of the output.

This completes our overview of the main calculations of the ARTop algorithm. We now present briefly the main analysis routines available in ARTop, that allow the user to evaluate the data easily with just a few lines of Python code.

4 ANALYSIS ROUTINES

The best way for a user to learn about the analysis routines of ARTop is to work through the guided examples that are provided in Jupyter notebooks that accompany the source code. In this section, we will focus on the core functionality of the analysis routines – the production of maps and time series.

In order to highlight the core features, we focus on AR11158 (SHARP 377). This region has been studied in many previous works (e.g. Jing et al. 2012; Tarr, Longcope & Millhouse 2013; Toriumi et al. 2013; Tziotziou, Georgoulis & Liu 2013; Kazachenko et al. 2015; Li & Liu 2015; Thalmann et al. 2019). The magnetograms of AR11158 have been downloaded from 22:00 UT on 2011 February 10 and last for 150 h. For what follows, the above starting time corresponds to hour zero in the plots and all times are reported in hours relative to this start time.

4.1 Maps

All the variables from Table 1 can be displayed as maps, and these maps are created by means of SunPy's Map class² (The SunPy Community 2020, (10.5281/zenodo.7582087)). Fig. 3 shows examples of maps at time $t = 60$ h.

4.2 Time series and flare analysis

The variables in Table 2 and their time-integrated versions can be displayed as time series. To do this, ARTop makes use of Pandas DataFrames³ which are highly portable.

Fig. 4 shows an example of such series for $d(\delta\mathcal{L})/dt$. In Fig. 4, the time series of $d(\delta\mathcal{L})/dt$ is displayed together with a running mean (μ_{30}) and an envelope of three standard deviations centred on the running mean ($\mu_{30} + 3\sigma$). The subscript corresponds to the number of time steps used in calculating the running mean. In this example, 30 time steps corresponds to 6 h of data. This parameter, as well as the height of the envelope, can be changed easily in ARTop.

²https://docs.sunpy.org/en/stable/guide/data_types/maps.html

³<https://pandas.pydata.org/>

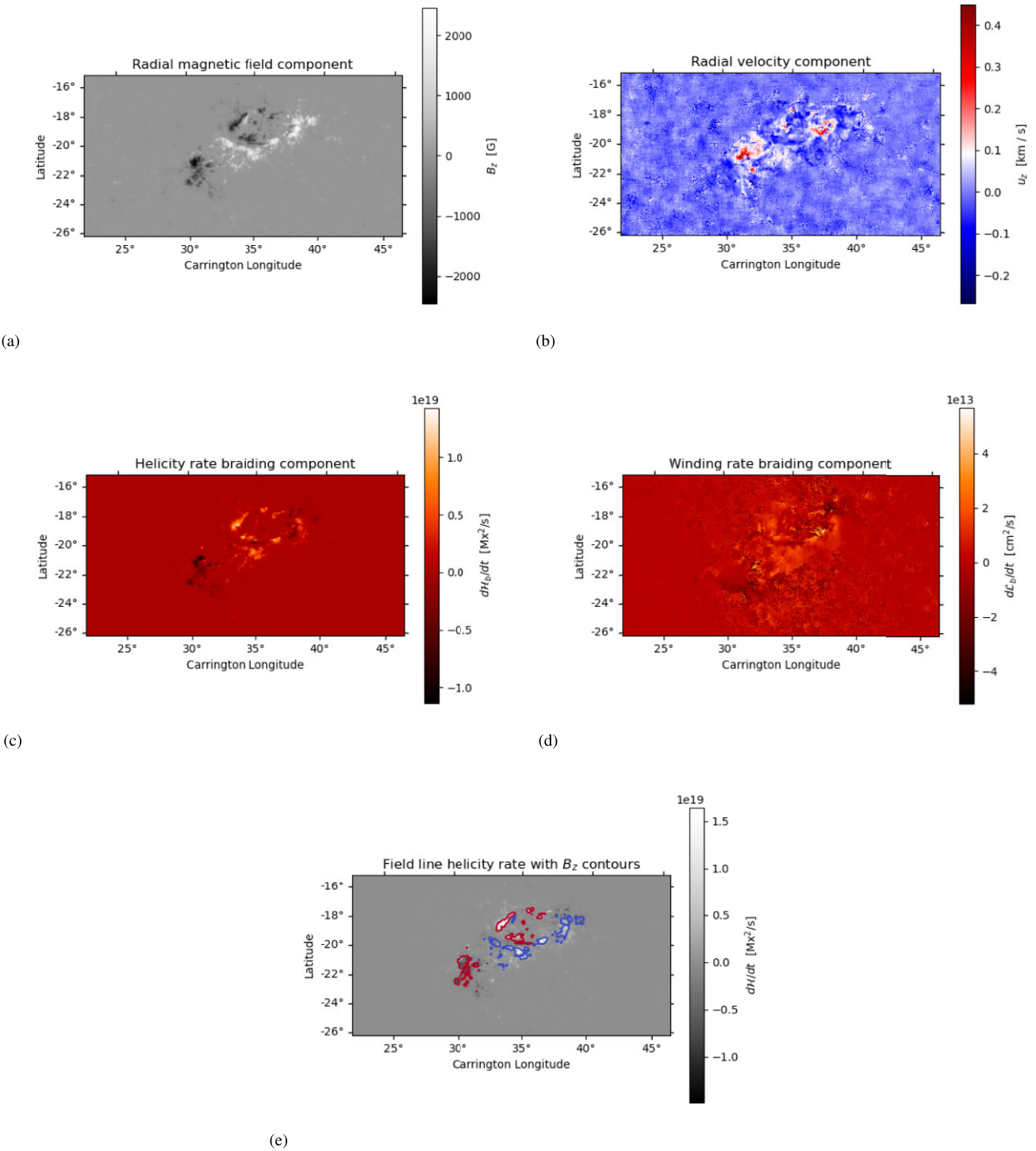


Figure 3 Maps, at $t = 60$ h, of (a) B_z , (b) u_z , (c) $d\mathcal{H}_b/dt$, (d) $d\mathcal{L}_b/dt$, and (e) $d\mathcal{H}/dt$ with contours of B_z (blue: +800 G, red: -800 G). The parameters (see Section 5 for definitions) used for the calculation are $CO = 50$, $VS = 20$, and $D = 1$. All colour scales are between minimum and maximum values.

One possible application of including the running mean and the envelope is to find a threshold condition that indicates the onset of solar flares. A possible signature of flare onset is for $d(\delta L)/dt$ to break through the envelope. Such a signature would signify a rapid and substantial change of complex field line topology at the photosphere, which is typical of many pre-flare scenarios (e.g. Joshi et al. 2011; Woods et al. 2017; MacTaggart & Fletcher 2019; Mitra, Joshi & Prasad 2020). In Fig. 4, the vertical black lines correspond

to recorded flare times. To find these times, ARTop makes use of information from the daily NOAA Space Weather Prediction Center reports on solar activity, which are downloaded from Solar Monitor.⁴ As well as flare times, these reports contain information about GOES X-ray events (the beginning, the maximum, and the end times of local

⁴<https://www.SolarMonitor.com>

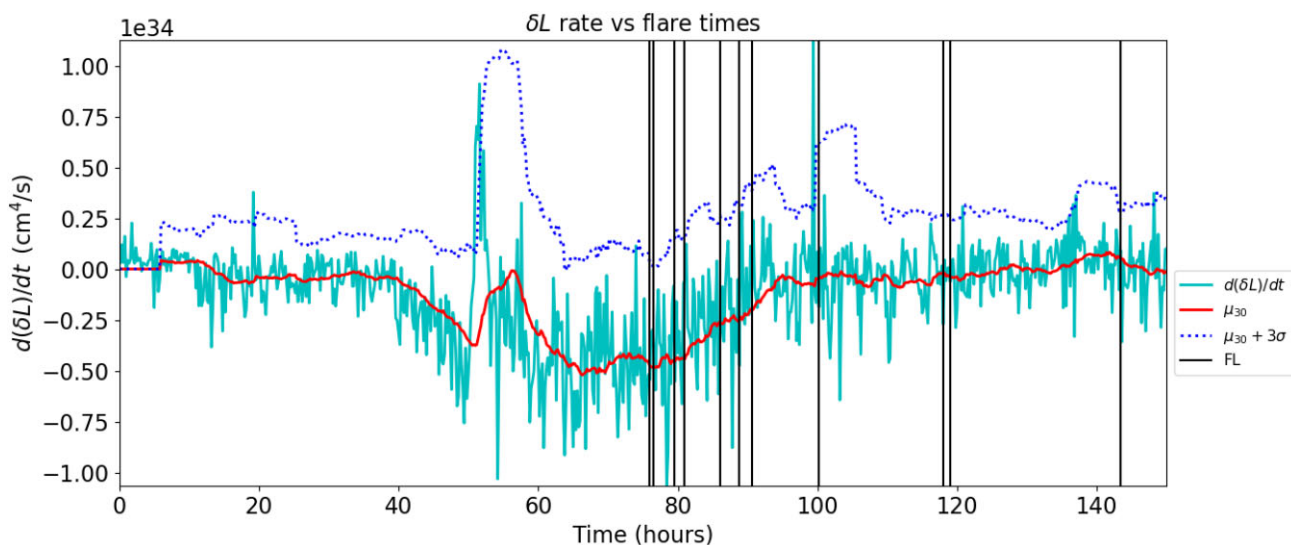


Figure 4 A time series of $d(\delta L)/dt$ together with a running mean μ_{30} , based on the past 6 h of data, and an envelope of 2.5 standard deviations. The vertical black lines correspond to recorded flare times in AR11158 (see the main text for more details). The calculation parameters are the same as those for Fig. 3.

peaks) and their strength classifications. Both flare and X-ray event times can be downloaded in ARTop and incorporated easily into time series plots such as that in Fig. 4.

Much detailed information can be found from these time series. For example, in Fig. 4, the rise just before $t = 50$ corresponds to the emergence of topologically complex magnetic field. This time marks the arrival of topologically complex magnetic field in the atmosphere and several flares follow this rise. Later there are several examples of the time series breaking through the envelope shortly before the onset of flares.

5 PARAMETERS

The calculations in ARTop are dependent on three user-controlled parameters: the magnetic field cut-off CO , the velocity smoothing window VS , and the downsampling factor D . The effect of changing CO has been discussed in MacTaggart et al. (2021), so we will only mention it here briefly. The effects of changing VS and D are discussed below. In particular, we will pay attention to how downsampling is incorporated into the calculations so that speed-up is gained without sacrificing significant accuracy.

5.1 Cut-off CO

The selected CO in ARTop imposes a lower limit on what magnetic field strengths are included in calculations. This is important in order to remove magnetic field that may be highly entangled but has very weak field strength, thus being irrelevant dynamically. In MacTaggart et al. (2021), it was shown how winding and helicity calculations behave in similar ways qualitatively as a function of varying CO . If CO is chosen to be too large ($> 100G$) there can be a large quantitative effect on the calculations. Previous tests, however, such as those in MacTaggart et al. (2021), suggest that qualitative behaviours, none the less, remain similar.

5.2 Velocity smoothing parameter VS

The VS parameter is related to the DAVE4VM method, it represents the number of surrounding pixels (the number VS) over which the

data are smoothed for the inversion to be well defined. Its value influences how smooth the derived velocity maps are. Descriptions of suitable choices are given in Schuck (2008). Examples of $VS = 12$ and 20 are provided in Fig. 5.

In Figs 5(a) and (b), we see comparisons of the time-integrated time series $L(t)$ and $H(t)$. There is very little qualitative difference, with the morphologies of the curves for each variable being very similar. Quantitative differences are much less than an order of magnitude.

For the δ -measures, displayed in Figs 5(c) and (d), the morphologies of the curves for the different VS are again very similar. There is a larger difference in magnitude for the majority of the time displayed, though this is still less than an order of magnitude. The difference increases at the very end of the displayed time, when the active region begins to move beyond 60° longitude, i.e. beyond the position in which projection effects can lead to substantial errors in calculations.

5.3 Downsampling factor D

The downsampling factor, D , is included to speed up calculations. This is an important feature if hundreds of active regions are to be studied, each with hundreds of time steps. In ARTop, downsampling is implemented in a particular way that aims to strike a balance between speed-up and the preservation of important topological features.

All of the helicity and winding fluxes depend on double integrals.⁵ In the inner integral, a point (field line) is chosen and the contribution to the winding/helicity flux of all other points (field lines) about this is calculated. The outer integral is then (at least numerically) the weighted sum of all these field line windings (compare equations (4) with (5) and (13) with (15)). Reducing the resolution of the magnetograms used for both the inner and outer integrals is too drastic and leads to qualitative changes in the output. Instead, we implement the following, which is illustrated in Fig. 6.

The inner integral, represented by the red grid in Fig. 6, is related to calculating the field line winding or helicity fluxes, dL/dt or

⁵Each integral is over an area, thus the total calculation of time derivatives involves integration over a 4D domain.

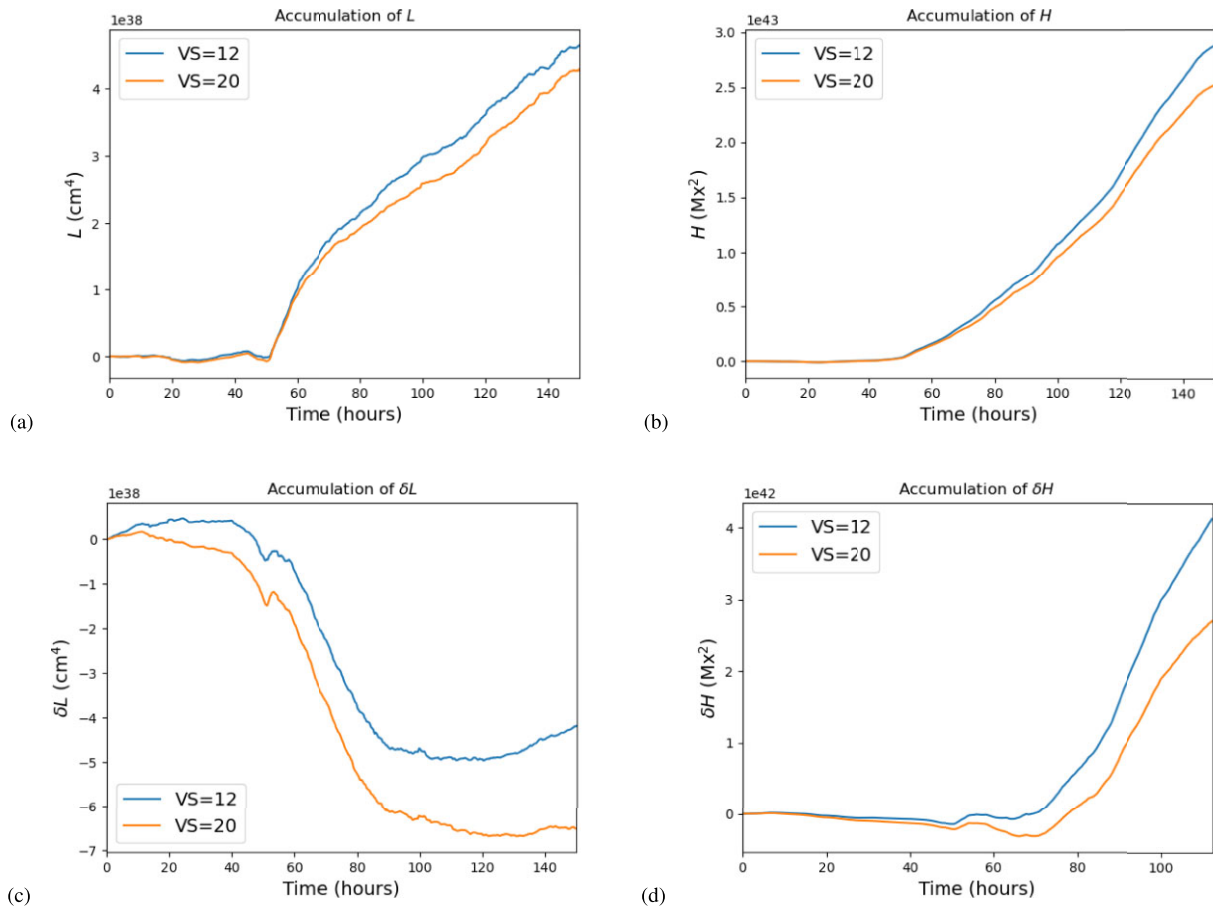


Figure 5 Comparisons of the effect of the velocity smoothing window parameter VS various of the quantities calculated by the ARTop code. Panels (a) and (b) are the total integrated winding L and helicity H , panels (c) and (d) the time-integrated metrics δL and δH .

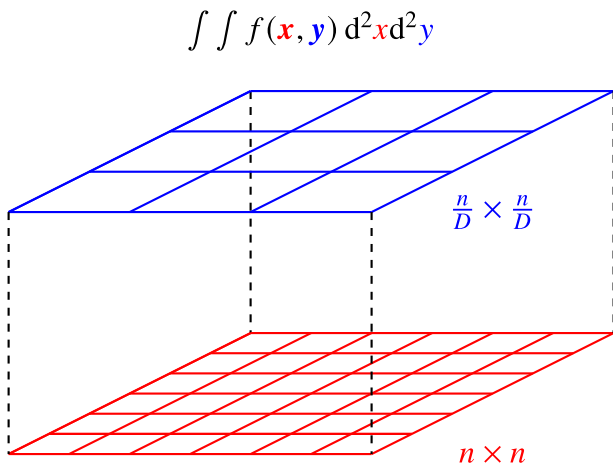


Figure 6 Downsampling in ARTop. The grids for each integral (inner and outer) are displayed. In each dimension, the resolution of the outer integral's grid (blue) is reduced by a factor D . The inner integral uses a grid (red) with the full resolution.

$d\mathcal{H}/dt$, which are always calculated on the full grid. For the outer integral, the number of points at which this calculation is performed is represented by the blue grid. In ARTop, selecting $D > 1$ results in a reduction of the blue outer grid (magnetogram) resolution for the outer integral by a factor of D in each dimension. Therefore,

although the number of points used to evaluate a particular flux is reduced, the value of the field line winding at each point still uses the full grid. In this way, important signatures of topological quantities can be preserved whilst also performing much faster calculations.

As an example of the practical effects of downsampling, we display how setting $D = 1, 2, 3, 5,$ and 10 affects the behaviour of δH and δL . These quantities are the time-integrated $d(\delta H)/dt$ and $d(\delta L)/dt$, respectively, and are an optional calculation in ARTop. The results are shown in Fig. 7.

One striking feature of the time series in Fig. 7 is that the morphologies of the curves for $D = 1, 2,$ and 3 are almost identical for the entire time span. The main difference is in the magnitude, and this is expected since each calculation uses different data (i.e. different pixels). A qualitative difference between the different time series is only strongly noticeable in δL for $D = 5, 10$. These large values would not be used in practice, but here they indicate that they can still produce accurate results for about 100 h of data representing different phases of complex dynamics.

As mentioned before, the main purpose of downsampling is to speed up calculations significantly without sacrificing important features of the time series. With the implementation described here, the theoretical speed-up should scale as $O(D^2)$. Normalizing with respect to the $D = 1$ (full resolution) case, the comparison of actual speed-ups to the theoretical values (for the cases shown in Fig. 7) and the normalized differences are displayed in Fig. 8. These results clearly show that significant speed-up can be achieved without sacrificing key features in the data.

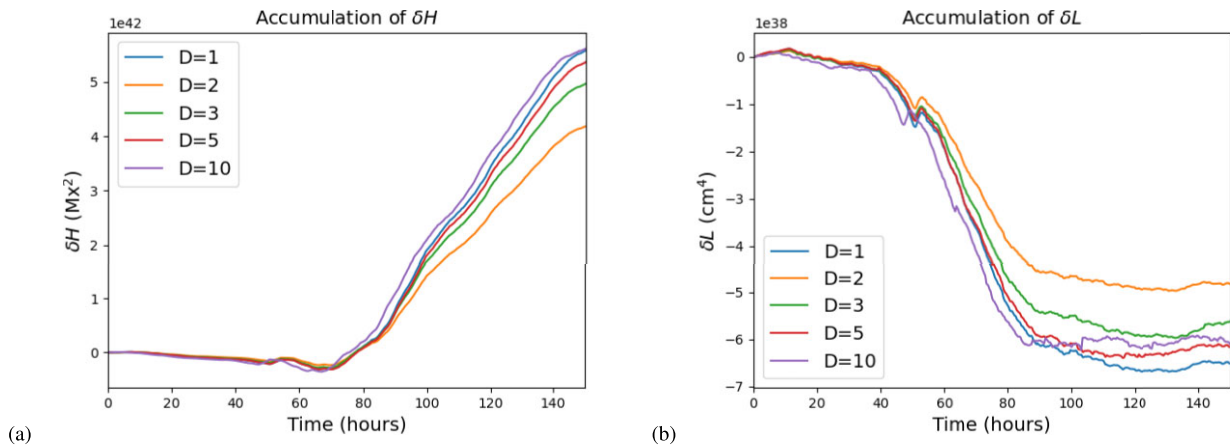


Figure 7 Plots of (a) δH and (b) δL versus time for different downsampling parameters $D = 1, 2, 3, 5$, and 10 .

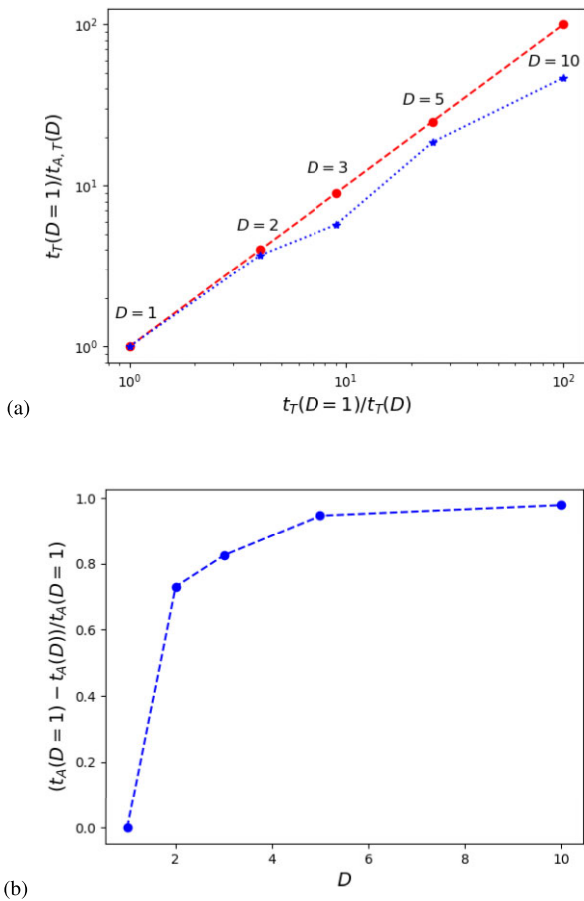


Figure 8 Two representations of how the run time (per snapshot) depends on D . Panel (a) shows a comparison of actual speed-ups (blue stars) compared to theoretical speed-ups (red dots). Downsampling values D are indicated beside each point. Subscripts T and A correspond to ‘theoretical’ and ‘actual’, respectively. Panel (b) shows the normalized difference with respect to $D = 1$.

5.4 Benchmarking/testing

The code has been checked against an existing IDL code (which is not publicly available) in MacTaggart et al. (2021), for active region AR11318, whose (braiding) helicity fluxes were calculated in Romano et al. (2014) using the IDL code. Although we found a small dif-

ference in the magnitudes (in part due to different methods of ‘cleaning’ the magnetograms), the morphology of the curves from ARTop and the code of Romano et al. (2014) were found to be very close.

To the best of our knowledge ARTop is currently the only publicly available helicity/winding flux calculation code, so further systematic benchmarking is not possible at this time. We hope that by publishing this code that situation can be altered. We note that the net helicity $H(t)$ calculated here for AR11158 yields very similar values to that of fig. 5(a) of Tziotziou et al. (2013), with magnitudes of the order of 10^{43} and a similar slope.

6 CONCLUSIONS

ARTop provides researchers with an effective tool for analysing topological quantities in solar active regions. The code has been tested in previous works and has proved to be very useful in identifying the topology of emerging structures (MacTaggart et al. 2021). The analysis routines of ARTop allow researchers to produce fast and detailed information about active region topology. In this paper, we have demonstrated ARTop’s analysis routines on a complex active region. We have discussed how parameters in the code affect the output and have shown that a particular implementation of downsampling can result in significant speed-ups without sacrificing the qualitative nature of the output.

The topological quantities in ARTop provide distinct and important information about magnetic field topology and, thus, about active region evolution. To use them effectively in the analysis of an active region, it is recommended that a researcher use them together and not in isolation. Although magnetic winding flux can provide more direct information about magnetic field topology, it is always useful to interpret its results together with helicity flux, in order to identify which signatures are important dynamically. Further, topological signatures, such as a steep rise in helicity/winding shortly before a flare, should be cross-checked with other variables, like u_z or S_z , in order to provide a deeper spatiotemporal picture of what they are conveying. This type of analysis can be performed simply in ARTop, making it an effective tool for solar active region research.

ACKNOWLEDGEMENTS

KA and DM acknowledge support from an Innovation Placement supported by the DiRAC HPC Facility as part of the DiRAC Federation Project. Funding for the DiRAC Federation Project was provided

by the URKI Digital Research Infrastructure programme. DM, CP, and BR welcome support from the US Air Force Office for Scientific Research (AFOSR): FA8655-20-1-7032. KA acknowledges support from the Aberdoc scheme. BR acknowledges the National Center for Atmospheric Research, which is a major facility sponsored by the National Science Foundation under cooperative agreement 1852977, and the financial support from NASA (NASA-LWS award 80NSSC20K0355, NASA-HSR award 80NSSC21K1676).

DATA AVAILABILITY

The code, with instructions on how to use it and produce plots, can be found at <https://github.com/DavidMacT/ARTop>.

REFERENCES

- Amari T., Luciani J. F., Aly J. J., Mikic Z., Linker J., 2003, *ApJ*, 585, 1073
- Berger M. A., 1988, *A&A*, 201, 355
- Berger M. A., 1993, *Phys. Rev. Lett.*, 70, 705
- Bobra M. G., Sun X., Hoeksema J. T., Turmon M., Liu Y., Hayashi K., Barnes G., Leka K., 2014, *Sol. Phys.*, 289, 3549
- Candelaresi S., Pontin D. I., Yeates A. R., Bushby P. J., Hornig G., 2018, *ApJ*, 864, 157
- Candelaresi S., Hornig G., MacTaggart D., Simitev R. D., 2021, *Commun. Nonlinear. Sci.*, 103, 106015
- Chae J., 2001, *ApJ*, 560, L95
- Chandra R.,ariat E., Schmieder B., Mandrini C. H., Uddin W., 2010, *Sol. Phys.*, 261, 127
- Démoulin P., Berger M. A., 2003, *Sol. Phys.*, 215, 203
- Gary G. A., 1989, *ApJS*, 69, 323
- Glogowski K., Bobra M. G., Choudhary N., Amezcu A. B., Mumford S. J., 2019, *J. Open Source Softw.*, 4, 1614
- Hoeksema J. T. et al., 2014, *Sol. Phys.*, 289, 3483
- Jeong H., Chae J., 2007, *ApJ*, 671, 1022
- Jing J., Park S.-H., Liu C., Lee J., Wiegelmann T., Xu Y., Deng N., Wang H., 2012, *ApJ*, 752, L9
- Joshi B., Veronig A. M., Lee J., Bong S.-C., Tiwari S. K., Cho K.-S., 2011, *ApJ*, 743, 195
- Kazachenko M. D., Fisher G. H., Welsch B. T., Liu Y., Sun X., 2015, *ApJ*, 811, 16
- LaBonte B. J., Georgoulis M. K., Rust D. M., 2007, *ApJ*, 671, 955
- Leka K. D., Barnes G., Crouch A. D., Metcalf T. R., Gary G. A., Jing J., Liu Y., 2009, *Sol. Phys.*, 260, 83
- Li A., Liu Y., 2015, *Sol. Phys.*, 290, 2199
- Liu Y., Schuck P. W., 2012, *ApJ*, 761, 105
- Liu Y., Team H. V. F., 2011, in Mansour N. N., Kosovichev A. G., Komm R., Longcope D., eds, *SDO-3: Solar Dynamics and Magnetism from the Interior to the Atmosphere*. Springer, New York, p. 91
- Liu Y., Hoeksema J. T., Bobra M., Hayashi K., Schuck P. W., Sun X., 2014, *ApJ*, 785, 13
- MacTaggart D., Fletcher L., 2019, *MNRAS*, 486, L96
- MacTaggart D., Prior C., 2021, *Geophys. Astrophys. Fluid Dyn.*, 115, 85
- MacTaggart D., Prior C., Raphaldini B., Romano P., Guglielmino S. L., 2021, *Nat. Commun.*, 12, 6621
- Metcalf T. R., 1994, *Sol. Phys.*, 155, 235
- Mitra P. K., Joshi B., Prasad A., 2020, *Sol. Phys.*, 295, 29
- Pariat E., 2020, in MacTaggart D., Hiller A., eds, *Topics in Magnetohydrodynamic Topology, Reconnection and Stability Theory (CISM Series)*, Vol. 591. Springer, Berlin, p. 145
- Pariat E., Démoulin P., Berger M. A., 2005, *A&A*, 439, 1191
- Park S.-H., Cho K.-S., Bong S.-C., Kumar P., Chae J., Liu R., Wang H., 2012, *ApJ*, 750, 48
- Prior C., MacTaggart D., 2019, *J. Plasma Phys.*, 85, 775850201
- Prior C., MacTaggart D., 2020, *Proc. R. Soc. Lond. Ser. A*, 476, 20200483
- Prior C., Yeates A. R., 2014, *ApJ*, 787, 100
- Romano P., Zuccarello F. P., Guglielmino S. L., Zuccarello F., 2014, *ApJ*, 794, 118
- Schuck P. W., 2008, *ApJ*, 683, 1134
- Tarr L., Longcope D., Millhouse M., 2013, *ApJ*, 770, 4
- Thalmann J. K., Moraitis K., Linan L., Pariat E., Valori G., Dalmasse K., 2019, *ApJ*, 887, 64
- The SunPy Community, 2020, *ApJ*, 890, 68
- Toriumi S., Iida Y., Bamba Y., Kusano K., Imada S., Inoue S., 2013, *ApJ*, 773, 128
- Tziotziou K., Georgoulis M. K., Liu Y., 2013, *ApJ*, 772, 115
- Tziotziou K., Park S.-H., Tsiropoula G., Kontogiannis I., 2015, *A&A*, 581, A61
- van Driel-Gesztelyi L., Green L. M., 2015, *Living Rev. Sol. Phys.*, 12, 1
- Vemareddy P., Démoulin P., 2017, *A&A*, 597, A104
- Woods M. M., Harra L. K., Matthews S. A., Mackay D. H., Dacie S., Long D. M., 2017, *Sol. Phys.*, 292, 38
- Yamamoto T. T., Kusano K., Maeshiro T., Yokoyama T., Sakurai T., 2005, *ApJ*, 624, 1072
- Yang S., Zhang H., Büchner J., 2009, *A&A*, 502, 333

SUPPORTING INFORMATION

Supplementary data are available at *RASSTAI* online.

ARTop-main.zip

Please note: Oxford University Press is not responsible for the content or functionality of any supporting materials supplied by the authors. Any queries (other than missing material) should be directed to the corresponding author for the article.

This paper has been typeset from a $\text{\TeX}/\text{\LaTeX}$ file prepared by the author.